Influence of the stratification in a hot water tank for thermal inertia improvment by latent heat thermal energy storage: a numerical study.

Alexis Iung, J.V. Simo Tala, Seyed Amir Bahrani, Mylène Deleglise-Lagardere

INFLUENCE OF THE STRATIFICATION IN A HOT WATER TANK FOR THERMAL INERTIA IMPROVMENT BY LATENT HEAT THERMAL ENERGY STORAGE: A NUMERICAL STUDY

Alexis IUNG [1, 2], Jules Voguelin SIMO TALA [2], S. Amir BAHRANI [2], Mylène LAGARDERE DELEGLISE [1]

[1] IMT Nord Europe, Institut Mines-Télécom, Univ. Lille, CERI Matériaux et Procédés, F-59000 Lille, France

[2] IMT Nord Europe, Institut Mines-Télécom, Univ. Lille, CERI Energie et Environnement, F-59000 Lille, France

ABSTRACT

The present study focusses on a parametric analysis on a composite-PCM structure aimed at enhancing the thermal storage capacity and inertia of a hot water tank. The inner surface of the tank comprises a conductive material (stainless steel) in direct contact with the stored hot water, while the outer surface is constructed using a combination of PCM and insulating material (Glass/PP composite). A constant temperature is considered on the conductive material surface, while the part exposed to the surroundings is assumed to be adiabatic. An organic PCM in solid-liquid state, specifically Rubitherm paraffin RT55, has been selected for this study. Previous research has identified PCM dimensions where the melting time approaches a constant value. The objective of this study is to investigate the impact of various temperature gradients on these parameters. Furthermore, the study has identified the presence of a maximum critical Fourier number and an optimal shape factor as the Stefan number tends towards infinity.

1. INTRODUCTION

Used to regulate large temperature variations, Latent Heat Thermal Energy Storage (LHTES) presents the best compromise between volume energy density and technological maturity. LHTES has gained popularity through the utilization of Phase Change Materials (PCMs). A solid-liquid PCM stores energy during the melting process and releases it during solidification (Sharma, 2009; Sharma, 2021).

PCMs are increasingly being employed in various technologies such as housing, electronics, solar devices, and hot water tanks. Mehling et al. (2003) demonstrated that installing a PCM module in a hot water tank allowed the water to be reheated and maintained at a set-point temperature four times longer, accounting for 1/16 of the total capacity. Cabeza et al. (2006) conducted a similar experiment by varying the quantity of PCM in order to increase the thermal density at the top of the hot water tank. They observed a 4% increase in thermal energy density for a temperature difference of 1°C and a 6% increase for a temperature difference of 8°C when using a PCM unit equivalent to 2% of the tank volume. Corresponding gains were 67% and 16% for a PCM unit equivalent to 6% of the tank volume. Bayomy et al. (2019) modeled a thermal collector and a domestic hot water storage system, where small PCM cylinders dispersed throughout the tank increased the collector efficiency for a single family from 35% to 82%. Wu et al. (2023) inserted PCM into the tank's outer side wall to create an insulating layer of the water tank. They found that the discharging time was 5 hours longer than a traditional water tank for a 30mm thickness, which is 10% longer.

Except for Wu et al., all of the above studies incorporated PCM into the tank rather than in the shell. A recent study by Iung et al. (2023) highlighted appropriate PCM dimensions where the melting time tends towards a constant value in an enhanced shell for hot water tank storage. The objective of this analysis is to investigate the influence of water tank temperature stratification modelled as successive wall temperature differences on these parameters. For each temperature difference, a dataset was created from a parametric study of PCM sizes. Results are presented using dimensional numbers such as the Rayleigh number, Fourier number, Aspect ratio, and Stefan number. After constructing correlations for each dataset, the previously identified appropriate parameters (dimensions and melting time) are examined to determine the influence of the Stefan number.

2. PROBLEM STATEMENT AND MATHEMATICAL FORMULATION

2.1 GEOMETRY DESCRIPTION

In the present study, a novel hot water tank design is introduced as illustrated in figure 1. The tank comprises a modified shell that is partitioned into individual enclosures with cylindro-annular walls. For the entirety of

10.18462.iir.pcm.2024.0011

the investigation, only one elementary enclosure is considered with symmetric boundary conditions. The composite geometric pattern of the cylindro-annular enclosure is defined in relation to the Phase Change Material (PCM). It consists of an insulating material serving as a liner/composite to seal the system, and a conductive material in the form of a U-shaped stainless steel structure filled with PCM from Rubitherm Gmbh (RT55 datasheet).

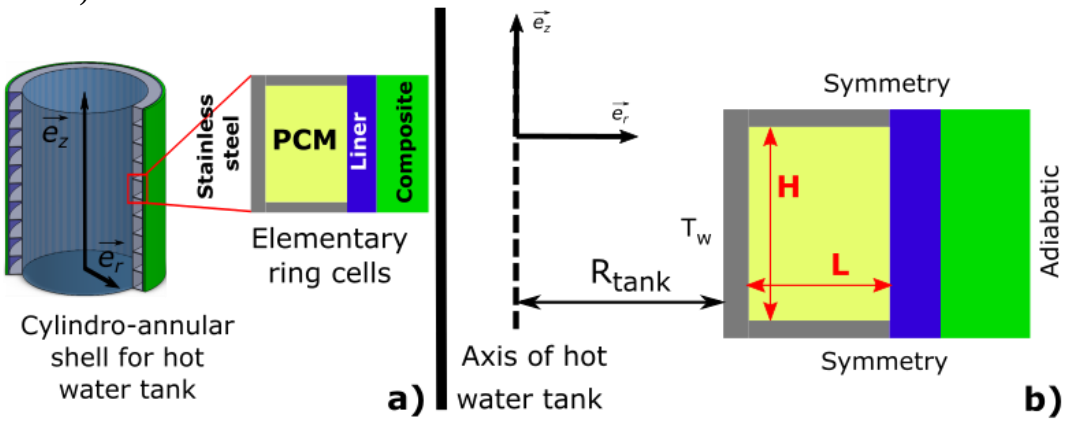

Figure 1: Illustration of the cylindro-annular enhanced shell for hot water tank (a), Computational domain and boundary conditions (b)

A polyurethane layer is added on the outer surface to insulate the tank and minimize heat loss. The composite material consists of 40% polypropylene (PP) and 60% UD glass fiber (GF). In this study, the composite material is considered homogeneous, and its properties are defined by the law of mixtures. Table 1 presents representative thermal characteristics of the materials utilized in the simulations.

Properties	Unity	Stainless steel	PP	GF	Composite	PCM
ρ_s	$\mathrm{kg.m^{-3}}$	8055	940	2520	188	880
ρ_l	$\mathrm{kg.m^{-3}}$	-	-	-	-	770
T_S	°	-	-	-	-	51
T_L	°	-	-	-	-	57
C_p	$\mathrm{J.kg^{-1}.K^{-1}}$	480	1700	787	1152.2	2000
$\mathrm{L_f}$	$\mathrm{kJ.kg^{-1}}$	-	-	-	-	170
λ	$\mathrm{W.m^{-1}.K^{-1}}$	15.1	0.2	1.1	0.39	0.2
β	$\mathrm{K^{-1}}$	-	-	-	-	1.1×10^{-4}
μ	Pa.s	-	-	-	-	0.03
A_{mush}	-	-	-	-	-	10^5

Table 1: Materials thermal properties (Tiari 2021, RT55, Star-CCM+)

2.2 MATHEMATICAL FORMULATION

The conservation equations governing the behaviour of the PCM over time and space include the continuity equation, momentum conservation equation, and energy conservation equation. In this study, a computational fluid dynamics (CFD) code Star-CCM+ is utilized with the specified geometry in 2D axisymmetric form. PCM can exist in three different states: liquid, solid, and the mushy zone, representing a two-phase mixture. Several assumptions are made in this analysis. It is assumed that the flow of liquid PCM is laminar and incompressible. The expansion of PCM volume during melting is neglected. To simulate buoyancy forces, the Boussinesq approximation is employed, and a user's field function is used to implement it as a momentum source term. With these assumptions, the conservation equations modelling the flow and heat transfer in the PCM are as follows:

- Continuity equation:

$$\frac{1}{r}\frac{\partial}{\partial r}(r\,u_r) + \frac{\partial u_z}{\partial z} = 0 \tag{1}$$

- Momentum equation:

$$\rho\left(\frac{\partial u_r}{\partial t} + u_r\frac{\partial u_r}{\partial r} + u_z\frac{\partial u_r}{\partial z}\right) = -\frac{\partial P}{\partial r} + \mu\left[\frac{1}{r}\frac{\partial}{\partial r}\left(r\frac{\partial u_r}{\partial r}\right) + \frac{\partial^2 u_r}{\partial z^2} - \frac{u_r}{r^2}\right] - A_{mush}\frac{(1-f_l)^2}{f_l^3+\varepsilon}u_r \tag{2}$$

$$\rho\left(\frac{\partial u_z}{\partial t} + u_r\frac{\partial u_z}{\partial r} + u_z\frac{\partial u_z}{\partial z}\right) = -\frac{\partial P}{\partial z} + \mu\left[\frac{1}{r}\frac{\partial}{\partial r}\left(r\frac{\partial u_z}{\partial r}\right) + \frac{\partial^2 u_z}{\partial z^2}\right] + \rho g\beta(T - T_m) - A_{mush}\frac{(1-f_l)^2}{f_l^3+\varepsilon}u_z \tag{3}$$

10.18462.iir.pcm.2024.0011

- Energy equation:

$$\rho\left(\frac{\partial h}{\partial t}+u_r\frac{\partial h}{\partial r}+u_z\frac{\partial h}{\partial z}\right)=\lambda\left[\frac{1}{r}\frac{\partial}{\partial r}\left(r\frac{\partial T}{\partial r}\right)+\frac{\partial^2 T}{\partial z^2}\right] \quad (4)$$

With the total enthalpy equation:

$$h=h_{ref}+\int_{T_i}^{T_w}C_p\,dT+f_l\,\mathrm{L_f} \quad (5)$$

And the liquid fraction:

$$f_l=\begin{cases}0 & if\ T<T_S\\ \frac{T-T_S}{T_L-T_S} & if\ T_S\le T\le T_L\\ 1 & if\ T>T_L\end{cases} \quad (6)$$

All these parameters will be presented in the nomenclature section.

2.3 BOUNDARY AND INITIAL CONDITIONS

At the beginning of the simulation, the left side of the stainless steel is subjected to a temperature T_w, while the initial temperature of the computational domain is set at T_i. A temperature difference $\Delta T = T_w - T_i$ is applied across the computational domain. Three cases of ΔT were considered: 9°C, 12°C and 18°C. It was assumed that the outside wall of the computational domain is insulated, and the right side of the composite part is subject to an adiabatic condition. Additionally, symmetry conditions were imposed on the upper and lower boundaries of the pattern. Each solid-solid interface ensures temperature and heat flux continuity, while the PCM-stainless steel interface accounts for conjugate heat transfer. The energy equation for the materials surrounding the PCM is expressed as follows for each material:

$$\rho_i C_{P,i}\frac{\partial T}{\partial t}=\lambda_i\left\{\frac{1}{r}\frac{\partial}{\partial r}\left(r\frac{\partial T}{\partial r}\right)+\frac{\partial^2 T}{\partial z^2}\right\} \quad (7)$$

Where i can stand for stainless steel, liner or composite material.

3. NUMERICAL PROCEDURE

3.1 VALIDATION OF THE CFD PROCEDURE

For this investigation, the finite volume approach was employed using the CFD code Star-CCM+ V15.06. The AMG algebraic solver and the SIMPLE algorithm were utilized to solve the conservation equations. Second-order discretization was applied to the convective terms of the momentum and energy equations. Temporal discretization involved applying 100 inner iterations of a second-order scheme.

The Hannoun benchmark (Hannoun, 2005) was utilized to validate the CFD code, serving as a reference solution for convection phase change problems. This benchmark assesses how well models can replicate temperature-dependent natural convection events during the melting of tin. Figure 3 depicts a comparison between the Star-CCM+ results and the benchmark findings. It illustrates the evolution of vorticity across several time intervals (100s, 200s, 450s, and 700s), revealing a qualitatively similar flow pattern between the benchmark and Star-CCM+ results. Additionally, the changes in liquid fraction over time were compared for the benchmark and CFD code findings. With a relative error of less than 0.9%, the Star-CCM+ results closely align with the benchmark data. The enthalpy-porosity model implemented in Star-CCM+, which includes the buoyancy source term, successfully reproduces the benchmark results, indicating the suitability of this CFD code for the remainder of the study.

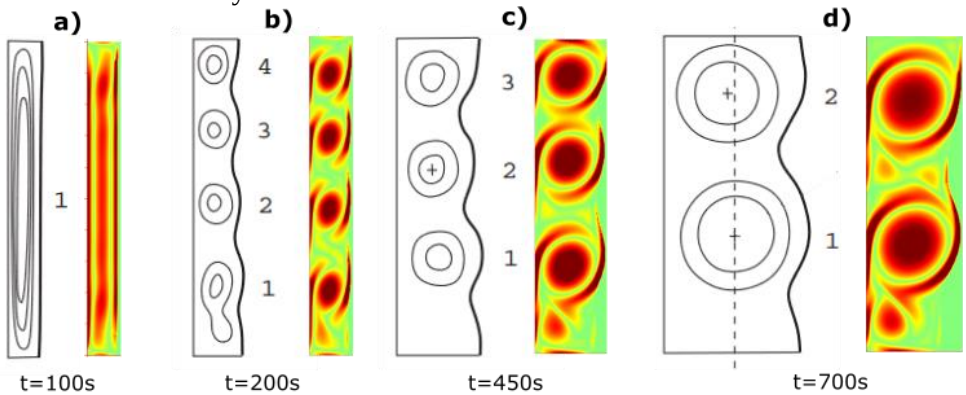

Figure 2: Comparison between Hannoun's benchmark (Hannoun, 2005) and the present CFD results

Two parametric studies were carried out simultaneously using Star-CCM+. The first study involved varying temperature differences: 9°C, 12°C, and 18°C. Subsequently, for each temperature difference, a parametric study on the height and length of the PCM enclosure was conducted. The thicknesses of the composite material, liner, and stainless steel were all kept constant. The dimensions of the computational domain were adjusted to correspond with the PCM's dimensions, with the height and length of the PCM ranging from 5 mm to 100 mm. Six height options and a minimum of three length values were considered, resulting in a total of 23 simulations for each temperature difference. The validity ranges for the study were set as H=[5,100] mm and L=[5,40]mm corresponding to a Rayleigh number range Ra=[159, 1 279 596].

3.2 GRID AND TIME STEP INDEPENDENCE ANALYSIS

The identical procedure as outlined in section 3.1 was employed. The computational domain from Fig.1b initial and boundary conditions described in section 2.3, and axisymmetric resolution were applied to simulate the melting of PCM RT55, a paraffin-based PCM from Rubitherm. To evaluate grid and time step independence during the PCM charging procedure, a computational domain measuring 20 mm in height and length was utilized.

Hexahedral elements were utilized throughout the entire computational domain. To accurately capture the thermal boundary layer and the interaction of heat transfer between the PCM and the surrounding shell, a mesh refinement was applied to the PCM region. For the grid independence analysis, five distinct grids with a total element count ranging from 12,178 to 188,052 were employed. The finest mesh with 188,052 elements served as the basis for subsequent grid investigations. Simulations were conducted for each mesh to calculate the liquid fraction and the heat flux on the conductive wall over time. These results were compared to data from the finest mesh to determine relative disparities. Generally, discrepancies decrease as the number of elements increases, albeit higher discrepancies are observed at the beginning and end of PCM melting. Taking these considerations into account, the grid with 120,888 elements was selected.

An examination of time independence was conducted using the selected grid. Five time steps, ranging from 0.05s to 1s, were evaluated with a reference time of 0.05s, similar to the mesh analysis. Relative errors were found to increase with the time step at the beginning of the simulation where temperature gradients are the strongest. However, after the initial few seconds, precision is largely unaffected, while the computational time increases significantly for smaller time steps. For the rest of the investigation, an adaptive time step for the first thirteen seconds was implemented, described as follows:

$$Time\ step = \begin{cases} 0.05\ s & if\ 0 < t < 1 \\ 0.1\ s & if\ 1 \leq t < 13 \\ 0.5\ s & if\ t \geq 13 \end{cases} \quad (8)$$

3.3 PRINCIPLE VARIABLES AND POST-PROCESSING PROCEDURE

Full cycle simulations of melting and solidification were investigated. A constant temperature was applied at the stainless steel wall with a constant and uniform initial temperature throughout the computational domain, corresponding to a temperature difference $\Delta T = T_w - T_i$. When the computational domain's final temperature reaches 99% of the wall temperature, the melting process is considered complete. The same temperature difference was applied for the solidification process but wall temperature and initial temperature were permuted. The solidification process is over when the final temperature of the computational domain reaches the new wall temperature.

The volume averaged liquid fraction and surface average heat flux on the stainless steel wall surface evolution over time were monitored in each CFD simulation. The determination of characteristic times throughout the entire cycle was made possible by these data. Four characteristic times are defined: PCM melting time t_{melt}, PCM solidification time t_{sol}, charging time t_{ch} and discharging time t_{dis}. Only melting time, which is the time required for the PCM to melt entirely and obtain a liquid fraction value of 1, was considered in the rest of the study. For the rest of the study, all the useful parameters were made dimensionless by using dimensional numbers as the Fourier number Fo, the Rayleigh number Ra, the aspect ratio AR and the Stefan number Ste. These numbers are defined in the nomenclature section.

4. RESULTS AND DISCUSSION

4.1. LOCAL ANALYSIS OF THE MELTING PROCESS

A complete cycle of melting and solidification is simulated, following the procedure outlined in section 3.3. For analysis purposes, only the melting process will be presented. Two PCM domains with the same length (20 mm) but differing heights (5 mm and 100 mm) will be compared to better understand the effect of the Rayleigh number. The four steps of the melting process, commonly acknowledged by authors in the literature

(Muhammad, 2017), are as follows: (1) transfer by pure conduction, (2) transfer by a combination of conduction and convection, (3) transfer by pure convection, and (4) solid shrinkage regime. Fig. 3 illustrates the liquid fraction for three different Stefan numbers at the various steps of the melting process. At the start of the procedure, the PCM is entirely solid. After a short while, a thin film of liquid appears on the stainless steel side. Regardless of the Rayleigh number, a symmetrical shape of the liquid fraction concerning the median horizontal plane is evident. This symmetry corresponds to a prevalence of pure conduction transfer. Following this stage, as the PCM's temperature continues to rise, two possible scenarios unfold. When the Rayleigh number is low, viscous effects outweigh buoyant effects, hindering the flow. To initiate natural convection, a larger volume of melted PCM is required. In such cases, the liquid fraction contour retains its symmetry relative to the horizontal median plane. Pure conduction remains the predominant heat transport mechanism, especially for a 5x20mm computational domain. Conversely, when the Rayleigh number is high, buoyancy effects overcome viscosity, leading to quicker natural convection and a more unimpeded flow. Moreover, an asymmetrical shape in the liquid fraction becomes noticeable. The primary mode of heat transfer here is a combination of convection and conduction. The flow velocity continues to increase in step 3. In regions with a low Rayleigh number, natural convection may begin due to this velocity increase. Consequently, for small Rayleigh numbers, convection has minimal impact on the melting process. The same observations and deductions as in the second stage can be applied to large Rayleigh numbers. However, convection predominates the melting process due to the significant rise in natural convection levels.

In the fourth stage, convection takes over as in the third stage, for both low and high values of Rayleigh number. As the PCM volume diminishes, the solid shrinkage regime of step 4 becomes apparent. The higher exchange surface to PCM volume ratio in smaller cavities results in a greater predominance of conduction, causing smaller cavities to melt more rapidly compared to larger ones.

In the initial step of the melting process, no discernible effect of the Stefan number on the computational domain was observed. Similarly, in the second step, for the 5x20 pattern, no significant variation due to the Stefan number was evident. However, for the 100x20 pattern, the Stefan number appeared to accelerate convection transfer. This effect became more pronounced in steps 3 and 4 for both patterns.

In summary, when the Rayleigh number is small, conduction predominates, while in the presence of a large Rayleigh number, convection becomes dominant. The Stefan number accelerates the melting process because a larger temperature difference increases the Rayleigh number, thereby enhancing the convection transfer.

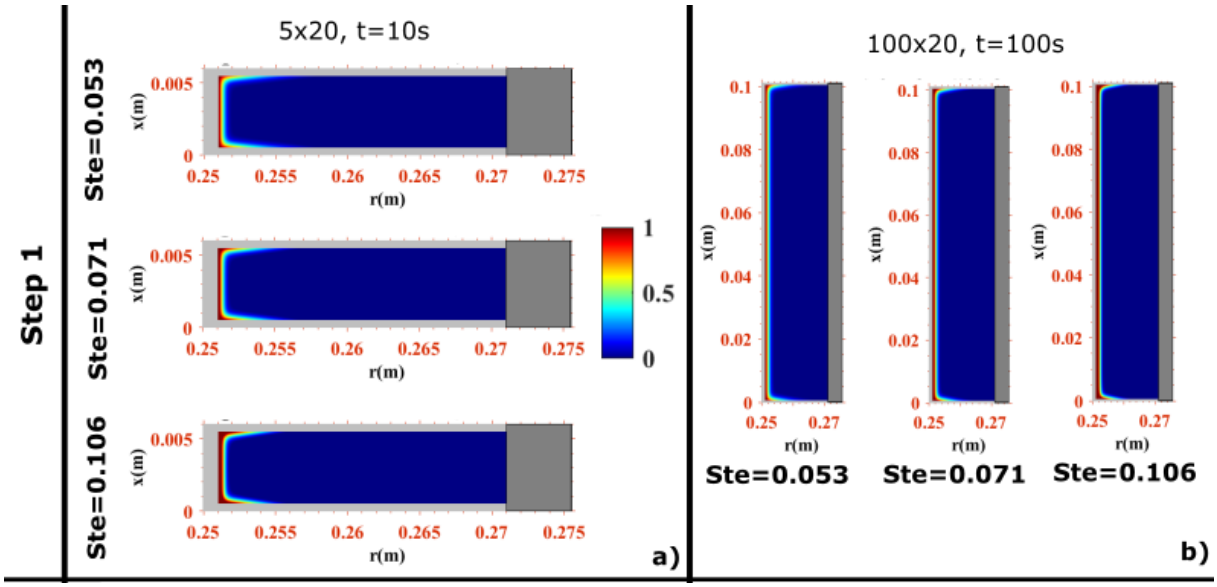

10.18462.iir.pcm.2024.0011

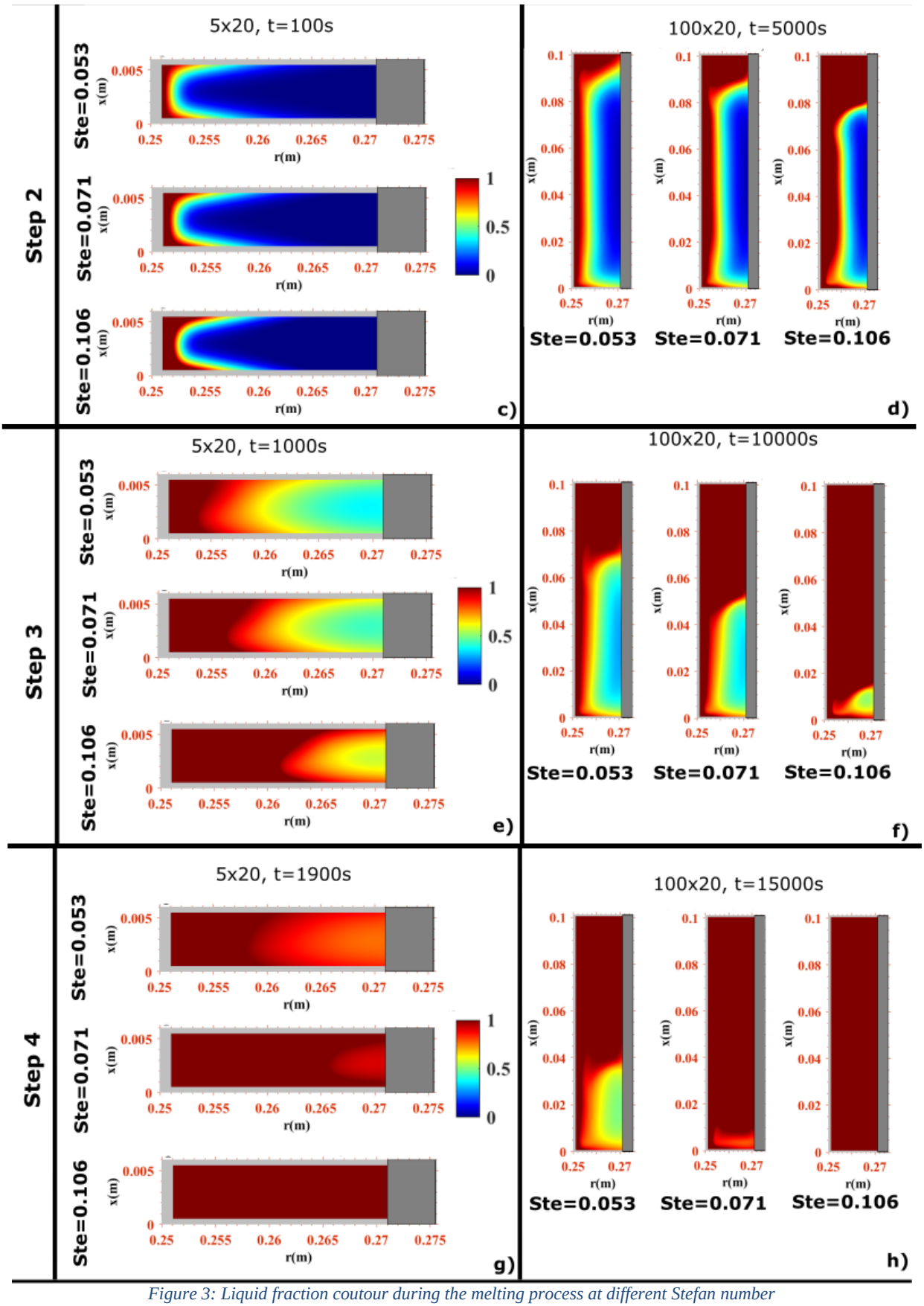

Figure 3: Liquid fraction coutour during the melting process at different Stefan number

4.2. DEVELOPMENT OF CORRELATION FOR MODELING THE MELTING PROCESS

In a previous study (Iung 2023), the melting Fourier number correlation for the computational domain of the present study was presented. The same methodology as described in this article was followed to develop the

correlation. A separate correlation was determined for each Stefan number, considering both cases of heat transfer: when conduction predominates and when convection predominates. These correlations depend on the Rayleigh number and aspect ratio. The authors (Iung 2023) defined the convective part of the correlation by:

$$Fo_{melt} = (6041\ Ra^{-0.65} + 9.55)(1 - \exp(4.93\ Ra^{-0.46} - 0.15)AR) \quad (9)$$

It was observed that for Rayleigh numbers $Ra \gtrsim 80\ 000$, an asymptotic limit is reached, and the convection part of the melting Fourier number correlation can be simplified to equation (10):

$$Fo_{melt} = Fo_{melt}^{crit}\left(1 - \exp(-b_{melt}\ AR)\right) \quad (10)$$

This equation, which solely depends on a geometrical parameter, is crucial for designing the hot water tank composed of an improved cylindro-annular shell housing a PCM. Two parameters have been identified in this equation:

- Fo_{melt}^{crit}, the critical melting Fourier number, is the highest Fourier number required for PCM to melt in this configuration and for a certain temperature difference.
- b_{melt}, the melting aspect ratio constant provides information on the optimal aspect ratio above which an increase in the Rayleigh number has no discernible impact on the PCM melting process.

Fo_{melt}^{crit} and b_{melt} have been determined by varying the applied temperature difference, i.e., the Stefan number. The values of these parameters have been summarized in Table 2:

Ste	Fo_{melt}^{crit}	b_{melt}
0.106	6.42	0.156
0.071	9.55	0.150
0.053	13.05	0.136

Table 2: Values of the critical melting Fourier number and the melting aspect ratio constant with respect to the Stefan number

Each parameter has been plotted and interpolated by a rational function as proposed by (Mastani Joybari 2019) with respect to the Stefan number.

$$Fo_{melt}^{crit} = \frac{2.14\ Ste + 0.33}{Ste - 0.019} \quad (11)$$

$$b_{melt} = \frac{0.161\ Ste - 0.0066}{Ste - 0.038} \quad (12)$$

The critical melting Fourier number decreases as the Stefan number increases. This implies that with a larger temperature difference, the melting time decreases, resulting in a quicker melting process for the PCM. The melting aspect ratio constant tends towards an asymptotic limit as the Stefan number increases. This indicates that the temperature difference influences the optimal size of the geometrical pattern. Therefore, as the Stefan number increases, the appropriate aspect ratio decreases, leading to a reduction in PCM height for a given PCM thickness.

A maximum critical melting Fourier number can be identified, with a value of 2.14. This corresponds to the limit of the critical melting Fourier number as the Stefan number tends to infinity. It suggests that melting reaches an asymptotic level when the temperature difference is very large. Similarly, a maximum melting aspect ratio of 0.161 is identified. The appropriate aspect ratio associated with this parameter decreases as a large temperature difference is applied.

5. CONCLUSION

The objective of this study was to analyze the influence of the stratification profile on a hot water tank with an improved cylindro-annular shell incorporating a specific PCM to enhance thermal inertia and stored energy. A parametric analysis on the size of the PCM revealed the existence of two dimensionless parameters for the tank: the critical melting Fourier number and the melting aspect ratio constant. By varying these parameters with respect to the Stefan number, correlations were established, and limiting factors were identified: the maximum critical melting Fourier number and the maximum melting aspect ratio. Each parameter corresponds to a melting Fourier number and an aspect ratio constant limit when the Stefan number tends towards infinity, i.e., when a large temperature difference is applied.

Based on these results, similar investigations could be conducted for the solidification process as during the solidification process, the PCM releases heat from liquid state above the liquidus temperature until complete solidification under the solidus temperature, to water contained by the tank.

6. REFERENCES

Sharma A, Tyagi V V, Chen C R, Buddhi D. 2009, Review on thermal energy storage with phase change materials and applications, *Renewable and Sustainable Energy Reviews*, 13(2): 318-345.

10.18462.iir.pcm.2024.0011

Sharma A, Chauhan R, Ali Kallioğlu M, Chinnasamy V, Singh T. 2021, A review of PCMs for thermal storage in solar air heating systems. *Materials Today: Proceedings*, 44: 4357-4363.

Mehling H, Cabeza L F, Hippeli S, Hiebler. 2003, PCM-module to improve hot water heat stores with stratification, *Renewable Energy*, 28(5): 699-711.

Cabeza L F, Ibáñez M, Solé C, Roca J, Nogués M. 2006, Experimentation with a water tank including a PCM module, *Solar Energy Materials and Solar Cells*, 90(9): 1273-1282.

Bayomy A, Davies S, Saghir Z. 2019, Domestic hot water storage tank utilizing PCMs: Numerical Approach, *Energies* 12(11): 2170.

Wu F, Qi C, Wang H, Li A, Li Z, Jiao X. 2023, An optimization study on the performance of hot water tank integrated phase change material, *Applied Thermal Engineering*, 223, 119983.

Star-CCM+ v15. 2020, User's guide.

RT55. Datasheet, available on: https://www.rubitherm.eu/media/products/datasheets/Techdata_-RT55_EN_09102020.PDF

Tiari S, Hockins A, Mahdavi M. 2021, Numerical study of a latent heat thermal energy storage system enhanced by varying configurations, *Case studies in thermal engineering*, 25: 10099.

Hannoun N, Alexiades V, Mai T Z. 2005, A reference solution for phase change with convection, *International Journal for Numerical Methods in Fluids*, Wiley Online Library.

Muhammad M D, Badr O. 2017, Performance of a finned, latent-heat storage system for high temperature applications, *Applied Thermal Engineering*, 116: 799-210.

Iung A, Simo Tala J V, Bahrani S. A, Lagardere Deleglise M. 2023, Etude numérique du stockage latent d'énergie thermique pour l'amélioration de l'inertie thermique d'un réservoir d'eau chaude sanitaire, *Proc. Congrès Français de Thermique SFT 2023*, 109-118.

Mastani Joybari M, Haghighat F, Seddegh S, Yuan Y. 2019, Simultaneous charging and discharging of phase change materiels: development of correlation for liquid fraction, Solar Energy, 188: 788-798.

7. NOMENCLATURE

Main notations

AR Aspect ratio, -, $AR = \frac{H}{L}$

A_{mush} Carman-Kozeny constant, -

C_p Specific heat capacity, $\mathrm{J.kg^{-1}.K^{-1}}$

f_l Liquid fraction, -

Fo Fourier number, -, $Fo = \frac{\alpha t}{L^2}$

g Gravity acceleration magnitude $g = 9.81\ m.s^{-2}$

H PCM cavity height, m

h Total enthalpy, J

$\mathrm{L_f}$ Latent heat, $J.kg^{-1}$

L PCM cavity length, m

P Pressure, Pa

Ra Rayleigh number, -, $Ra = \frac{g\beta(T_w - T_m)H^3}{\alpha\nu}$

r, z Cylindrical coordinates, m

Ste Stefan number, -, $Ste = \frac{C_p(T_w - T_m)}{\Delta h}$

S^m Carman-Kozeny source term, -

T Temperature, $°K$

t Time, s

u_r, u_z Velocity components, $m.s^{-1}$

Greek symbols

α Thermal diffusivity, $m^2.s$

β Thermal expansion coefficient, K^{-1}

ε Small numerical coefficient, $\varepsilon = 0.001$

ρ Density, $kg.m^{-3}$

λ Thermal conductivity, $W.m^{-1}.K^{-1}$

ν Kinematic viscosity, $m^2.s^{-1}$

μ Dynamic viscosity, $Pa.s$

Subscripts

i Initial

L Liquidus

$melt$ Melting

m Mean

S Solidus

w wall

8. ACKNOWLEGMENTS

This work is supported by the Corenstock Industrial Chair ANR-20-CHIN-0004-01, cofounded by elm.leblanc, IMT and its schools IMT Nord Europe and Mines Saint-Etienne. Funded by the French National Research Agency, the project is also endorsed by the Institut Carnot Télécom & Société Numérique and accredited by the EMC2 cluster.

10.18462.iir.pcm.2024.0011